

Teraelectronvolt pulsed emission from the Crab Pulsar detected by MAGIC

S. Ansoldi¹, L. A. Antonelli², P. Antoranz³, A. Babic⁴, P. Bangale⁵, U. Barres de Almeida^{5,26}, J. A. Barrio⁶, J. Becerra González^{7,27}, W. Bednarek⁸, E. Bernardini⁹, B. Biasuzzi¹, A. Biland¹⁰, O. Blanch¹¹, S. Bonnefoy⁶, G. Bonnoli², F. Borracci⁵, T. Bretz^{12,28}, E. Carmona¹³, A. Carosi², P. Colin⁵, E. Colombo⁷, J. L. Contreras⁶, J. Cortina¹¹, S. Covino², P. Da Vela³, F. Dazzi⁵, A. De Angelis¹, G. De Caneva⁹, B. De Lotto¹, E. de Oña Wilhelmi¹⁴, C. Delgado Mendez¹³, F. Di Pierro², D. Dominis Prester⁴, D. Dorner¹², M. Doró¹⁵, S. Einecke¹⁶, D. Eisenacher Glawion¹², D. Elsaesser¹², A. Fernández-Barral¹¹, D. Fidalgo⁶, M. V. Fonseca⁶, L. Font¹⁷, K. Frantzen¹⁶, C. Fruck⁵, D. Galindo¹⁸, R. J. García López⁷, M. Garczarczyk⁹, D. Garrido Terrats¹⁷, M. Gaug¹⁷, N. Godinović⁴, A. González Muñoz¹¹, S. R. Gozzini⁹, Y. Hanabata¹⁹, M. Hayashida¹⁹, J. Herrera⁷, K. Hirotani²⁰, J. Hose⁵, D. Hrupec⁴, G. Hughes¹⁰, W. Idec⁸, H. Kellermann⁵, M. L. Knoetig¹⁰, K. Kodani¹⁹, Y. Konno¹⁹, J. Krause⁵, H. Kubo¹⁹, J. Kushida¹⁹, A. La Barbera², D. Lelas⁴, N. Lewandowska¹², E. Lindfors^{21,29}, S. Lombardi², F. Longo¹, M. López⁶, R. López-Coto¹¹, A. López-Oramas¹¹, E. Lorenz⁵, M. Makariev²², K. Mallot⁹, G. Maneva²², K. Mannheim¹², L. Maraschi², B. Marcote¹⁸, M. Mariotti¹⁵, M. Martínez¹¹, D. Mazin¹⁹, U. Menzel⁵, J. M. Miranda³, R. Mirzoyan⁵, A. Moralejo¹¹, P. Munar-Adrover¹⁸, D. Nakajima¹⁹, V. Neustroev²¹, A. Niedzwiecki⁸, M. Nevas Rosillo⁶, K. Nilsson^{21,29}, K. Nishijima¹⁹, K. Noda⁵, R. Orito¹⁹, A. Overkemping¹⁶, S. Paiano¹⁵, M. Palatiello¹, D. Paneque⁵, R. Paoletti³, J. M. Paredes¹⁸, X. Paredes-Fortuny¹⁸, M. Persic^{1,30}, J. Poutanen²¹, P. G. Prada Moroni²³, E. Prandini^{10,31}, I. Puljak⁴, R. Reinthal²¹, W. Rhode¹⁶, M. Ribó¹⁸, J. Rico¹¹, J. Rodríguez García⁵, T. Saito¹⁹, K. Saito¹⁹, K. Satalecka⁶, V. Scalzotto¹⁵, V. Scapin⁶, C. Schultz¹⁵, T. Schweizer⁵, S. N. Shore²³, A. Sillanpää²¹, J. Sitarek¹¹, I. Snidaric⁴, D. Sobczynska⁸, A. Stamerra², T. Steinbring¹², M. Strzys⁵, L. Takalo²¹, H. Takami¹⁹, F. Tavecchio², P. Temnikov²², T. Terzić⁴, D. Tesaro⁷, M. Teshima⁵, J. Thaele¹⁶, D. F. Torres²⁴, T. Toyama⁵, A. Treves²⁵, J. Ward¹¹, M. Will⁷, and R. Zanin¹⁸

(Affiliations can be found after the references)

Received 29 June 2015 / Accepted 20 October 2015

ABSTRACT

Aims. We investigate the extension of the very high-energy spectral tail of the Crab Pulsar at energies above 400 GeV.

Methods. We analyzed ~320 h of good-quality Crab data obtained with the MAGIC telescope from February 2007 to April 2014.

Results. We report the most energetic pulsed emission ever detected from the Crab Pulsar reaching up to 1.5 TeV. The pulse profile shows two narrow peaks synchronized with those measured in the GeV energy range. The spectra of the two peaks follow two different power-law functions from 70 GeV up to 1.5 TeV and connect smoothly with the spectra measured above 10 GeV by the Large Area Telescope (LAT) on board the *Fermi* satellite. When making a joint fit of the LAT and MAGIC data above 10 GeV the photon indices of the spectra differ by 0.5 ± 0.1 .

Conclusions. Using data from the MAGIC telescopes we measured the most energetic pulsed photons from a pulsar to date. Such TeV pulsed photons require a parent population of electrons with a Lorentz factor of at least 5×10^6 . These results strongly suggest IC scattering off low-energy photons as the emission mechanism and a gamma-ray production region in the vicinity of the light cylinder.

Key words. gamma rays: stars – pulsars: individual: Crab pulsar – stars: neutron

1. Introduction

The Crab Pulsar, PSR J0534+220, is a young neutron star (NS) with a rotational period of 33 ms. It was created after the supernova explosion SN1054. The Crab is the most powerful pulsar in our Galaxy, with a spin-down luminosity of 4.6×10^{38} erg s⁻¹. It is one of the few pulsars that has been detected across the electromagnetic spectrum from radio up to gamma rays, and is one of the brightest at high energies (HE, $0.1 < E < 10$ GeV; Fierro et al. 1998; Kuiper et al. 2001; Abdo et al. 2010; Aliu et al. 2008). The recent discovery of pulsed emission at energies

up to 400 GeV (Aliu et al. 2011; Aleksić et al. 2012a) highlights the exceptional qualities of this source.

The Crab Pulsar emission profile is characterized by three components: two pulses separated by ~0.4 in phase observed at all energies from centimeter radio ($E \sim 10^{-4}$ eV) to very high-energy gamma rays (VHE, $E > 100$ GeV), and a third component, the Bridge, which is defined as the pulse phase between the main pulse and the second pulse. The main pulse (P1) has the highest intensity at radio frequencies and defines phase 0; the second pulse (P2), which is often referred to as the interpulse, is weaker at radio frequencies. The amplitude

of each pulse depends on the energy (Kuiper et al. 2001); in particular, in the gamma-ray regime, P2 becomes dominant above 25–50 GeV, whereas the Bridge is only detected up to 150 GeV (Aleksić et al. 2014).

The HE gamma-ray emission from pulsars is believed to be produced via synchrotron-curvature radiation by electron-positron pairs moving along curved paths inside the light cylinder. The maximum photon energy is limited by either magnetic and gamma-gamma pair absorption or radiation losses, resulting in spectral cutoffs at around a few GeV (Cheng et al. 1986). This theoretical scenario has been confirmed by the analysis of about 150 pulsars detected by the *Fermi*-LAT gamma-ray telescope (Abdo et al. 2013). The observed pulse profiles and spectral shapes suggest that the gamma-ray beams have a fan-like geometry and that they are located at high-altitude zones inside the magnetosphere towards the spin equator, either close to the light cylinder (LC, outer gap models; Cheng et al. 1986; Romani & Yadigaroglu 1995; Cheng et al. 2000; Takata et al. 2006) or along the last open magnetic field lines (slot gap models; Arons 1983; Muslimov & Harding 2004).

The first year of *Fermi*-LAT observations of the Crab Pulsar spectrum validates the consensus view of a spectral cutoff at $(5.8 \pm 0.5_{\text{stat}} \pm 1.2_{\text{syst}})$ GeV (Abdo et al. 2010). However, the gamma-ray emission later discovered at VHE (Aliu et al. 2011; Aleksić et al. 2011, 2012a) is not compatible (at more than a 6σ confidence level) with flux predictions based on synchro-curvature emission. This new and unexpected spectral component, described by a steep power-law function (with a photon index of approximately 3.5) between 25 and 400 GeV required an ad hoc explanation (Aliu et al. 2011; Aleksić et al. 2011, 2012a). Some of the advocated models include the same synchro-curvature mechanism responsible for the sub-TeV emission, although under extreme conditions (Bednarek 2012; Viganò & Torres 2015), whereas others proposed that a new mechanism is at work, namely inverse Compton (IC) scattering on seed photon fields (from infrared to X-rays). In the case of IC radiation, different VHE gamma-ray production regions have been considered from the acceleration gap in the pulsar magnetosphere (Aleksić et al. 2011; Hirotani 2011; Lyutikov et al. 2012; Harding & Kalapotharakos 2015) to the ultra-relativistic cold wind that extends from the light cylinder to the wind shock (Aharonian et al. 2012; Bogovalov & Aharonian 2000; Mochol & Pétri 2015).

The goal of this work is to investigate the maximum energy reached in the Crab Pulsar spectrum. For this purpose, we re-analyzed more than 300 h of excellent-quality data of the Crab recorded by MAGIC from 2007 to 2014 in stand-alone and in stereoscopic mode.

2. Observations and analysis

MAGIC is an array of two imaging atmospheric Cherenkov telescopes (IACTs) designed for the detection of gamma rays in the energy band between few tens of GeV and few tens of TeV. It is located in the Canary Islands (Spain) on La Palma at 2250 m above sea level. The two telescopes have a reflective surface that is 17 m in diameter and fine pixelated cameras with a 3.5° field of view.

MAGIC started its operations in stand-alone mode with the first MAGIC telescope, MAGIC-I, in autumn 2004. In February 2007, its readout system was upgraded to an ultra-fast FADC of 2 GHz sampling rate (Goebel et al. 2008), which allowed a better reconstruction of the timing characteristics of the recorded images and a factor of two background reduction.

The upgraded MAGIC-I could detect sources with fluxes as low as 1.6% of the Crab Nebula flux above 280 GeV in 50 h of observation (Aliu et al. 2009). It had an energy resolution of 20% at around 1 TeV. Observations carried out during this initial phase will be referred to in the following as “mono” observations. In 2009, MAGIC became a stereoscopic system leading to an improvement in sensitivity of a factor of 2 (Aleksić et al. 2012b). To equalize the performance and hardware of the two telescopes, a major upgrade was carried out during the summers of 2011 and 2012. First, the readout systems of both telescopes were upgraded with the domino ring sampler version 4 chip; in the following year, the MAGIC-I camera was replaced by a uniformly pixelated one, a clone of the second telescope camera (Aleksić et al. 2016a). Currently the array has an energy threshold as low as ~ 70 GeV for low zenith angle observations and an integral sensitivity above 300 GeV of 0.6% of the Crab Nebula flux in 50 h of observation (Aleksić et al. 2016b). The energy resolution is 15–17% at ~ 1 TeV.

The analysis was performed with the standard MAGIC software, MARS (Moralejo et al. 2010). The gamma/hadron separation and the estimation of the gamma-ray direction make use of random forest (RF) algorithms (Albert et al. 2008; Aleksić et al. 2010). The energy estimation can be performed either by means of the RF technique or with Monte Carlo (MC) lookup tables (LUTs), which are the standard procedures for mono and stereo data analysis, respectively. In the case of the Crab Pulsar above ~ 100 GeV the background is no longer dominated by hadrons, but gamma rays from the Crab Nebula. Therefore, we applied background rejection cuts specifically optimized for a gamma-dominated background and specified that at least 90% of our MC gamma rays survive those cuts. The cut optimization is based on the maximization of the modified formula (17) by Li & Ma (1983) which considers as background the hadronic and nebula events derived from the nebula excess and the power-law spectrum for the pulsar found in Aleksić et al. (2012a). For the differential energy spectra, we applied an unfolding procedure correcting for the energy bias and the detector finite energy resolution. We tested the five unfolding methods described in Albert et al. (2007) and verified their consistency within statistical errors. The upper limits (ULs) to the differential flux were obtained by following the Rolke et al. (2005) method under the assumption of a Gaussian background and 20% systematic uncertainty in the flux level. Hereafter, the ULs will be given at 95% confidence level (CL). The pulsar rotational phase of each event was defined by using the TEMPO2 package (Hobbs et al. 2006, and cross-checked by our own code, Moya 2006) and the monthly ephemeris publicly provided by the Jodrell Bank Observatory¹ (Lyne et al. 1993).

In this work we used all the data taken in stereoscopic mode, until April 2014, when pointing at the Crab. The selected sample includes observations performed at zenith angles up to 70° . To increase the statistics we also reanalyzed Crab mono data recorded after the upgrade of the readout system (between 2007 and April 2009) at zenith angles smaller than 30° . Both mono and stereo data samples were taken partially in the “on” position and partially in false-source tracking mode (Fomin et al. 1994), the latter pointing at two symmetric positions 0.4° from the source. Data affected by hardware problems and bad atmospheric conditions or showing unusual hadron rates were removed from the analyzed data sample resulting in 97 h and 221 h of effective time for the mono and the stereo samples, respectively. Given that the considered data sample

¹ <http://www.jb.man.ac.uk/research/pulsar/crab.html>

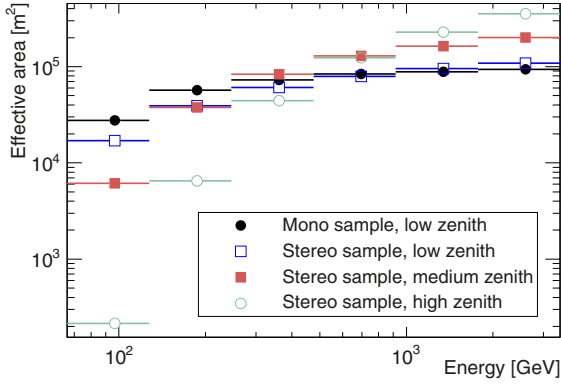


Fig. 1. Effective area after background rejection cuts of four representative data subsamples.

spans seven years with different instrument performance, we created nine analysis periods each with its corresponding MC simulation. The whole data sample was then further subdivided into three zenith angle ranges to better account for the corresponding dependence of the image shower parameters at the cut optimization stage. This resulted in 19 data subsamples, each period with at least some low zenith angle data used to monitor the instrument performance; the RF matrices and energy LUTs were produced separately. Figure 1 shows the effective area of four representative datasets: mono, and stereo in the three zenith angle ranges. The differential energy spectra obtained for each independent analysis were combined later on, after weighting with the exposure and when applying the unfolding procedure.

3. Results

3.1. Light curve

In the search for pulsation above 400 GeV the Crab Pulsar we defined the phase ranges of the two peaks according to the results obtained in our previous studies (Aleksić et al. 2012a, 2014): the main peak P1 $\in (-0.017-0.026)$ and the interpulse P2 $\in (0.377-0.422)$. The interval $(0.52-0.87)$ was considered an off-pulse region (Fierro et al. 1998) where we estimated the background to be subtracted from the histograms.

Figure 2 shows the folded pulse profile that we obtained between 100 and 400 GeV and above 400 GeV with 318 h of observation. In the 100–400 GeV energy range P1 is detected with a significance level of 2.8σ , whereas P2 at 5.6σ after Li & Ma (1983, Eq. (17)). The statistical significance of the detection of P1 and P2 with this analysis is smaller than that reported in Aleksić et al. (2014) with less than half of the observation time; the analysis presented in this work combines many periods with different sensitivities and energy thresholds, and these factors contribute to decreasing the signal-to-noise ratio at the lowest energies, hence worsening the overall signal significance. If we consider only stereo data for zenith angles below 35° , which identify the data subsample with the lowest energy threshold and best gamma/hadron separation at the lowest energies, we end up with 152 h of observation time, yielding a signal significance of 6.6σ and 8.8σ for P1 and P2, respectively, in the energy range between 100 and 400 GeV. This is in agreement with the results reported in Aleksić et al. (2014) for the 50–400 GeV energy range. Beyond 400 GeV (above the energy threshold of the 19 analyses used here) the gamma/hadron separation is efficient for all the analyses and we have a clear gain in the signal significance for the combined sample due to the increase in

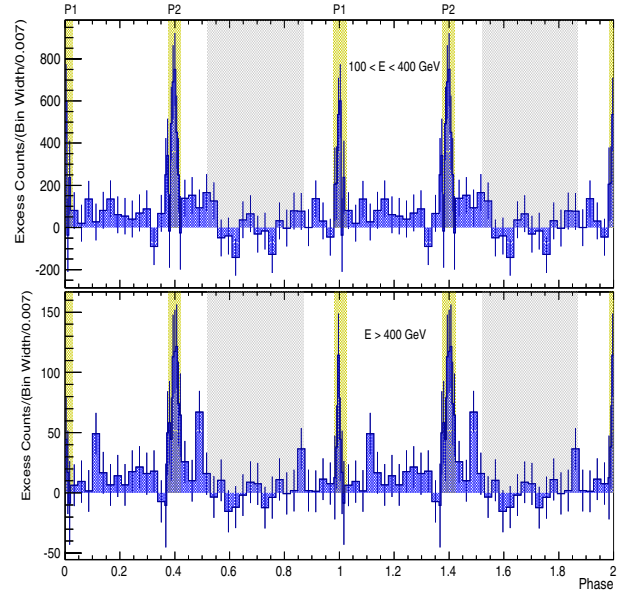


Fig. 2. Pulse profile of the Crab Pulsar between 100 and 400 GeV (*upper panel*) and above 400 GeV (*bottom panel*). The pulse profile, shown twice for clarity, is background subtracted. The bin width around the two peaks is 4 times smaller (0.007) than the rest (0.027) in order to highlight the sharpness of the peaks. Yellow dashed areas identify the phase intervals of the two peaks, whereas the gray areas show the off-pulse region.

Table 1. Number of excess events and corresponding significance of P1 and P2 for different energy ranges in ~ 320 h of data.

| Energy range [GeV] | P1 | | P2 | |
|-----------------------|-----------------|--------------|-----------------|--------------|
| | N_{ex} | Significance | N_{ex} | Significance |
| 100–400 | 1252 ± 442 | 2.8σ | 2537 ± 454 | 5.6σ |
| >400 | 188 ± 88 | 2.2σ | 544 ± 92 | 6.0σ |
| >680 | 130 ± 66 | 2.0σ | 293 ± 69 | 4.3σ |
| >950 | 119 ± 54 | 2.2σ | 190 ± 56 | 3.5σ |

photon statistics. For energies above 400 GeV, only P2 is significantly detected. The total number of excess events are 544 ± 92 and 188 ± 88 for P2 and P1, respectively, corresponding to 6σ and 2.2σ for each peak. With a higher energy cut at 500 GeV, meant to exclude the lower energy events from the light curve where no spillover correction is applied, P2 is still detected at 5σ while P1 shows a 2σ signal with 418 ± 104 and 152 ± 108 excess events, respectively. Table 1 summarizes the number of excess events with their corresponding significance for different integral energy ranges.

The significance of the pulsation was also tested with the H-test (de Jager et al. 1989), which does not make any a priori assumptions on the position and the shape of the pulsed emission, resulting in a 3.5 (2.8) σ significance above 400 (500) GeV.

We fitted the pulse profile above 400 GeV to a more finely binned distribution with two symmetric Gaussian functions (as in Aleksić et al. 2012a). The available statistics does not allow us to consider more complicated functions. P1 and P2 are located at the phases $0.9968 \pm 0.0020_{\text{stat}} + 0.0055_{\text{sys}} - 0.0048_{\text{sys}}$ and $0.4046 \pm 0.0035_{\text{stat}} + 0.0047_{\text{sys}} - 0.0074_{\text{sys}}$, respectively, in agreement with the positions found at lower energies between 50 and 400 GeV (Aleksić et al. 2012a). The full width at half maximum (FWHM) for P1 is $0.010 \pm 0.003_{\text{stat}} + 0.003_{\text{sys}} - 0.010_{\text{sys}}$ and for P2 is $0.040 \pm 0.009_{\text{stat}} + 0.005_{\text{sys}} - 0.008_{\text{sys}}$.

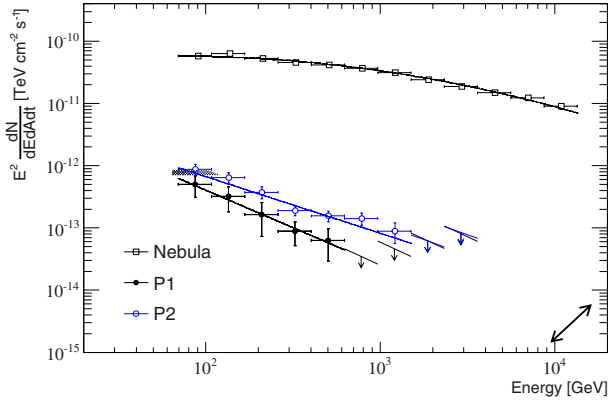


Fig. 3. Phase-folded SED of the Crab P1 (black circles) and P2 (blue circles) measured by MAGIC between ~ 70 GeV and 1.5 TeV. The butterfly identifies the systematic uncertainty on the flux normalization and spectral index, whereas the arrow on the bottom right corner corresponds to an energy shift of 17%. The Crab Nebula spectrum (open squares) is also shown for comparison. The differential flux upper limits at 95% CL are computed under the assumption of the power-law spectrum measured in this work.

The systematic uncertainty on the estimation of the peak positions reflects the precision of the pulsar ephemerides used for this analysis, taking into account the RMS of the timing noise, the uncertainty on the arrival time of the first pulse taken as reference, and the error introduced by the barycentric corrections. It also includes the effect of the histogram binning. The width of the peaks beyond this energy is compatible within the errors with the value measured below 400 GeV. We note that the results reported above 400 GeV for P1 are obtained for a $\sim 2\sigma$ signal and should be taken with caution. For comparison, the best-fit P1 and P2 positions in the 100 MeV to 10 GeV energy range are 0.9915 ± 0.0005 and 0.3894 ± 0.0022 (Abdo et al. 2010).

3.2. Energy spectra

Figure 3 shows the phase-folded spectral energy distributions (SED) of P1 and P2 from ~ 70 GeV up to 1.5 TeV, obtained by using the Bertero unfolding method (Bertero 1989). Both the differential energy spectra are described well by power-law functions with a photon index α of $3.2 \pm 0.4_{\text{stat}} \pm 0.3_{\text{sys}}$ and $2.9 \pm 0.2_{\text{stat}} \pm 0.3_{\text{sys}}$ for P1 and P2, respectively. The results of the fits, shown in Table 2 for a normalization energy at 150 GeV (the decorrelation energy is 120 GeV and 190 GeV for P1 and P2, respectively), are in agreement with our earlier results (Aleksić et al. 2012a, 2014). In the case of P2, the power-law spectrum extends up to 1.5 TeV, whereas P1 cannot be measured beyond 600 GeV. At energies above the last obtained spectral point, we computed ULs to the differential flux at 95% CL under the assumption of the power-law spectrum found in this work. However, a 20% change in the photon index yields a variation of less than 15% in the UL. These ULs do not constrain any possible cutoff given the current sensitivity of the instrument. The spectral points and ULs are listed in Table 3.

The extrapolation of the MAGIC energy spectra to lower energies agrees within the statistical errors with the spectra measured with *Fermi*-LAT above 10 GeV, which were already showing a deviation from the expected exponential cutoff (Aleksić et al. 2014). A joint correlated- χ^2 -fit² of MAGIC and

² The fit takes into account the correlation between the MAGIC spectral points due to the unfolding procedure.

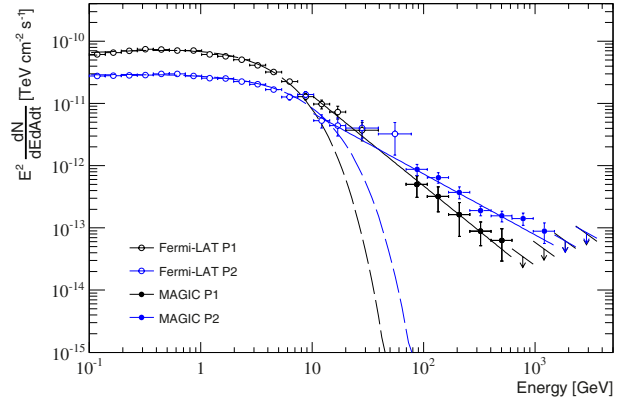


Fig. 4. Phase-folded SED of the Crab P1 (black circles) and P2 (blue circles) at HE and VHE (open and filled circles). The results of the power law with exponential cutoff fits to the *Fermi*-LAT points are shown by dashed lines (Aleksić et al. 2014), whereas the joint *Fermi*-LAT/MAGIC fits to power-law functions above 10 GeV are shown by solid lines. The upper limits to the differential flux at 95% CL are computed under the assumption of the power-law spectrum found in this work, as represented by the slope of the arrows.

Table 2. Results of the spectral fit to a power-law function. Errors indicate 1σ statistical uncertainties. E_0 indicates the normalization energy.

| | | E_0 [GeV] | f_{E_0} [TeV ⁻¹ cm ⁻² s ⁻¹] | α | $\chi^2/\text{d.o.f.}$ |
|------------------------------|----|----------------|--|---------------|------------------------|
| MAGIC | P1 | 150 | $(1.1 \pm 0.3) \times 10^{-11}$ | 3.2 ± 0.4 | 0.3/3 |
| | P2 | 150 | $(2.0 \pm 0.3) \times 10^{-11}$ | 2.9 ± 0.2 | 5.4/5 |
| <i>Fermi</i> -LAT & MAGIC | P1 | 50 | $(5.3 \pm 0.8) \times 10^{-10}$ | 3.5 ± 0.1 | 1.5/6 |
| | P2 | 50 | $(5.7 \pm 0.6) \times 10^{-10}$ | 3.0 ± 0.1 | 8.4/9 |

Table 3. Spectral points of the MAGIC measurements shown in Fig. 3.

| Energy [GeV] | Bin Center [GeV] | P1 $E^2 dN/dE dAdt$ [TeV cm ⁻² s ⁻¹] $\times 10^{-13}$ | P2 $E^2 dN/dE dAdt$ [TeV cm ⁻² s ⁻¹] $\times 10^{-13}$ |
|-----------------|---------------------|--|--|
| 69–108 | 87 | 5.0 ± 1.9 | 8.7 ± 1.8 |
| 108–167 | 135 | 3.2 ± 1.4 | 6.5 ± 1.2 |
| 167–259 | 210 | 1.6 ± 0.9 | 3.7 ± 0.8 |
| 259–402 | 325 | 0.9 ± 0.4 | 1.9 ± 0.3 |
| 402–623 | 504 | 0.6 ± 0.3 | 1.6 ± 0.3 |
| 623–965 | 781 | <0.3 | 1.4 ± 0.3 |
| 965–1497 | 1211 | <0.5 | 0.9 ± 0.3 |
| 1497–2321 | 1879 | <0.6 | <0.6 |
| 2321–3598 | 2914 | <0.8 | <0.8 |

Fermi-LAT spectral points above 10 GeV shows that the new spectral components are described well ($\chi^2/\text{n.d.f.} = 1.5/6$ and $\chi^2/\text{n.d.f.} = 8.5/9$ for P1 and P2, respectively) by simple power-law functions (see Table 2), where the normalization energy is set to 50 GeV. The photon indices of the two power-law functions are $\alpha = 3.5 \pm 0.1$ and $\alpha = 3.0 \pm 0.1$ for P1 and P2, respectively. The difference in the spectral slopes by $\Delta\alpha = 0.5 \pm 0.1$ is significant by more than 3σ , indicating that the intensity of P1 drops more rapidly with energy than that of P2. At X-ray energies (3–10 keV) *NuSTAR* detected a similar spectral behavior with P2 harder than P1 and the corresponding photon indices of 1.66 ± 0.02 and 1.80 ± 0.01 , respectively (Madsen et al. 2015).

A fit to a power-law function plus exponential cutoff allows us to impose a lower limit on the spectral cutoff of 700 GeV at 95% CL. The measured spectral difference at VHE could be naturally explained either by two distinct production locations for each peak or by the difference in the phase-resolved spectrum of X-rays which act as targets for IC scattering.

We cross-checked the P2 energy spectrum by comparing the mono data to the stereo data and found that the results were stable within statistical errors for all the considered unfolding methods. We also computed the Crab Nebula SED, as shown in Fig. 3 (open squares), using the subsample of the data taken in wobble mode. The nebula spectral measurement was obtained by analyzing the same energy range as the pulsar analysis, using the same energy binning and gamma selection cuts. The resulting spectral points are consistent with the results presented in [Aleksić et al. \(2012b, 2015\)](#). Therefore, we assumed that no extra systematic uncertainty on the total flux is needed for this specific analysis. These systematic uncertainties are 17% on the energy scale, 19% on the flux normalization, and 0.3 on the photon index. The last error is the only one not in agreement with [Aleksić et al. \(2012b\)](#) and mainly arises from the larger uncertainty of the unfolding given the low statistics of the result.

4. Discussion and conclusions

The new results presented here probe the Crab Pulsar as the most compact TeV accelerator known to date. The remarkable detection of pulsed emission up to 1.5 TeV revealed by MAGIC imposes severe constraints on where and how the underlying electron population produces gamma rays at these energies. The electron population responsible for the VHE emission should have Lorentz factors greater than 5×10^6 , which can be responsible for the VHE emission only when accelerated near or beyond the light cylinder ([Bogovalov 2014](#)). The TeV pulsed emission cannot be produced with synchro-curvature radiation, even in the extreme case in which the magnetic-field-aligned electric field approaches the strength of the magnetic field. In this scenario, the curvature radius would have to be one order of magnitude larger than the typical one, which is believed to be between 0.3 and 2 times the light cylinder radius ([Viganò et al. 2015](#)) (for further discussions on this issue we refer to [Kalapotharakos et al. 2014](#); [Harding & Kalapotharakos 2015](#), and references therein). Therefore, the unprecedented measurement of pulsed emission extending up to TeV energies performed with the MAGIC telescopes implies that the IC process is at work in the Crab Pulsar, and that it dominates the emission of gamma rays above 50 GeV. This partially solves the puzzle posed by the previous published results, but also opens new challenges. We note that although other processes (e.g. synchro-curvature radiation) could account for the production of 100–400 GeV photons, the simple power-law function obtained by a joint fit of *Fermi*-LAT and MAGIC data from ~ 10 GeV up to 1.5 TeV suggests a single mechanism for both P1 and P2, and that this must be Compton up-scattering of soft photons off high-energy electrons.

Concerning IC scattering, two scenarios which were previously proposed to explain the VHE emission below 400 GeV can be considered: the magnetospheric synchrotron-self-Compton model ([Aleksić et al. 2011](#)) and the IC in the pulsar wind region model ([Aharonian et al. 2012](#)). The former assumes that there are acceleration gaps in the outer magnetosphere ([Cheng et al. 1986, 2000](#); [Romani & Yadigaroglu 1995](#); [Takata et al. 2006](#); [Arons 1983](#); [Muslimov & Harding 2004](#)) where primary positrons propagate outwards and escape, and are then illuminated by a strong magnetospheric infrared (IR) photon field

which is then up-scattered by positrons to TeV-scale energies. These primary TeV photons are then efficiently absorbed by the same IR field and materialize as secondary e^\pm pairs with GeV to several TeV energies. These secondary pairs are created at a greater distance where there is a lower photon-field density near and outside the LC, and can up-scatter the IR-UV photons into 10 GeV–5 TeV photons (via synchrotron self-Compton process, [Hirotani 2013](#)). Some of them escape from the magnetosphere and are observable from Earth. However the synchronization of the pulse profile in the GeV and TeV regimes limits this interpretation, suggesting a similar region of generation where absorption of TeV photons is unavoidable. The measured time delay between the best-fit peak positions in the MeV–GeV and the TeV regime is $178 \pm 69 \mu\text{s}$ and $512 \pm 139 \mu\text{s}$ for P1 and P2, respectively, which – when considering the relatively large systematics in the determination of the peak positions – are compatible with the hypothesis of no separation between the bulk of the radiation region where all these photons are generated (neglecting more complicated geometrical effects and assuming the simple case of stationary emission regions).

The pulsar wind scenario considers the IC scattering off the synchrotron, pulsed IR, and X-ray photons by the particles (electron/positron) of the cold relativistic wind. It is commonly accepted that the pulsar wind is magnetically dominated near the LC. Thus, in the wind model, the wind becomes abruptly particle-kinetic-energy dominated over a short distance (compared to the dimension of the wind region). Based on previous results by Cherenkov telescopes on the Crab Pulsar ([Aliu et al. 2011](#); [Aleksić et al. 2012a](#)), this distance was estimated to be 20–50 LC radii ([Aharonian et al. 2012](#)). In this narrow cylindrical zone, electrons and positrons are rapidly accelerated up to Lorentz factors of 5×10^5 . The bulk Lorentz factor is assumed to display a power-law dependence on the distance, $\Gamma(R) = \Gamma_0 + (\Gamma_w - \Gamma_0) \left(\frac{R-R_0}{R_f-R_0} \right)^\alpha$, where Γ_0 and Γ_w are the initial and the maximum wind Lorentz factors, R_0 the distance at which the acceleration starts, R_f the distance at which Γ_w is reached, and the power-law index $\alpha \sim 1, 3, 10$ ([Aharonian et al. 2012](#)). To obtain a Γ_w compatible with the value derived from the detection of TeV photons ($\sim 5 \times 10^6$), the region in which particles are accelerated has to extend to a much larger radius than the one considered in [Aharonian et al. \(2012\)](#). In this case however, the model fails to reproduce the spectral shape below 100 GeV ([Aharonian et al. 2012](#), figure SM1). Instead, a slower and continuous acceleration (e.g., due to magnetic reconnection) or a more complex radial dependence could be at play. Other approaches in the context of the pulsar wind emission region and/or pulsar magnetosphere are currently being investigated to try to give a satisfactory explanation to the TeV pulsed emission ([Mochol & Pétri 2015](#); [Harding & Kalapotharakos 2015](#)). So far, all the existing models have failed to reproduce the narrow peaks ([Aleksić et al. 2011](#); [Aharonian et al. 2012](#)) observed in the Crab Pulsar light curve above 400 GeV, keeping the coherence along four decades in energy. The MAGIC results require a revision of the state-of-the-art models proposed to explain how and where gamma-ray pulsed emission from 100 MeV to 1.5 TeV are produced.

Acknowledgements. We would like to thank the Instituto de Astrofísica de Canarias for the excellent working conditions at the Observatorio del Roque de los Muchachos in La Palma. The financial support of the German BMBF and MPG, the Italian INFN and INAF, the Swiss National Fund SNF, the ERDF under the Spanish MINECO (FPA2012-39502), and the Japanese JSPS and MEXT is gratefully acknowledged. This work was also supported by the Centro de Excelencia Severo Ochoa SEV-2012-0234, CPAN CSD2007-00042,

and MultiDark CSD2009-00064 projects of the Spanish Consolider-Ingenio 2010 programme, by grant 268740 of the Academy of Finland, by the Croatian Science Foundation (HrZZ) Project 09/176 and the University of Rijeka Project 13.12.1.3.02, by the DFG Collaborative Research Centers SFB823/C4 and SFB876/C3, and by the Polish MNiSzW grant 745/N-HESS-MAGIC/2010/0.

References

- Abdo, A. A., Ackermann, M., Ajello, M., et al. 2010, *ApJ*, **708**, 1254
- Abdo, A. A., Ajello, M., Allafort, A., et al. 2013, *ApJS*, **208**, 17
- Aharonian, F. A., Bogovalov, S. V., & Khangulyan, D. 2012, *Nature*, **482**, 507
- Aliu, E., Aliu, E., Anderhub, H., et al. 2007, *Nucl. Instr. Methods*, **583**, 494
- Albert, J., Aliu, E., Anderhub, H., et al. 2008, *Nucl. Instr. Methods*, **588**, 424
- Aleksić, J., Antonelli, L. A., Antoranz, P., et al. 2010, *A&A*, **524**, A77
- Aleksić, J., Alvarez, E. A., Antonelli, L. A., et al. 2011, *ApJ*, **742**, 43
- Aleksić, J., Alvarez, E. A., Antonelli, L. A., et al. 2012a, *A&A*, **540**, A69
- Aleksić, J., Alvarez, E. A., Antonelli, L. A., et al. 2012b, *Astropart. Phys.*, **35**, 435
- Aleksić, J., Ansoldi, S., Antonelli, L. A., et al. 2014, *A&A*, **565**, L12
- Aleksić, J., Ansoldi, S., Antonelli, L. A., et al. 2015, *J. High Energy Astrophys.*, **5**, 30
- Aleksić, J., Ansoldi, S., Antonelli, L. A., et al. 2016a, *Astropart. Phys.*, **72**, 61
- Aleksić, J., Ansoldi, S., Antonelli, L. A., et al. 2016b, *Astropart. Phys.*, **72**, 76
- Aliu, E., Anderhub, H., Antonelli, L. A., et al. 2008, *Science*, **322**, 1221
- Aliu, E., Anderhub, H., Antonelli, L. A., et al. 2009, *Astropart. Phys.*, **30**, 293
- Aliu, E., Arlen, T., et al. (VERITAS Collaboration) 2011, *Science*, **334**, 69
- Arons, J. 1983, *ApJ*, **266**, 215
- Bednarek, W. 2012, *MNRAS*, **424**, 2079
- Bertero, M. 1989, *Advances in Electronics and Electron Physics* (New York: Academic Press), 75, 1
- Bogovalov, S. V. 2014, *MNRAS*, **443**, 2197
- Bogovalov, S. V., & Aharonian, F. A. 2000, *MNRAS*, **313**, 504
- Cheng, K. S., Ho, C., & Ruderman, M. 1986, *ApJ*, **300**, 500
- Cheng, K. S., Ruderman, M., & Zhang, L. 2000, *ApJ*, **537**, 964
- de Jager, O. C., Raubenheimer, B. C., & Swanepoel, J. W. H. 1989, *A&A*, **221**, 180
- Fierro, J. M., Michelson, P. F., Nolan, P. L., & Thompson, D. J. 1998, *ApJ*, **494**, 734
- Fomin, V. P., Stepanian, A. A., Lamb, R. C., et al. 1994, *Astropart. Phys.*, **2**, 137
- Goebel, F., Bartko, H., Carmona, E., et al. 2008, *Int. Cosmic Ray Conf.*, **3**, 1481
- Harding, A. K., & Kalopotharakos, C. 2015, *ApJ*, **811**, 63
- Hirovani, K. 2011, *ApJ*, **733**, L49
- Hirovani, K. 2013, *ApJ*, **766**, 98
- Hobbs, G. B., Edwards, R. T., & Manchester, R. N. 2006, *MNRAS*, **369**, 655
- Kalopotharakos, C., Harding, A. K., & Kazanas, D. 2014, *ApJ*, **793**, 97
- Kuiper, L., Hermsen, W., Cusumano, G., et al. 2001, *A&A*, **378**, 918
- Li, T.-P., & Ma, Y.-Q. 1983, *ApJ*, **272**, 317
- Lyne, A. G., Pritchard, R. S., & Graham-Smith, F. 1993, *MNRAS*, **265**, 1003
- Lyutikov, M., Otte, N., & McCann, A. 2012, *ApJ*, **754**, 33
- Madsen, K. K., Reynolds, S., Harrison, F., et al. 2015, *ApJ*, **801**, 66
- Mochol, I., & Pétri, J. 2015, *MNRAS*, **449**, L51
- Moralejo, R. A., Gaug, M., Carmona, E., et al. 2010, MARS: The MAGIC Analysis and Reconstruction Software (Astrophysics Source Code Library)
- Moya, M. L. 2006, Ph.D. Thesis, Fac CC Fisicas, UCM
- Muslimov, A. G., & Harding, A. K. 2004, *ApJ*, **606**, 1143
- Rolke, W. A., López, A. M., & Conrad, J. 2005, *Nucl. Instr. Meth. Phys. Res. A*, **551**, 493
- Romani, R. W., & Yadigaroglu, I.-A. 1995, *ApJ*, **438**, 314
- Takata, J., Shibata, S., Hirovani, K., & Chang, H.-K. 2006, *MNRAS*, **366**, 1310
- Viganò, D., & Torres, D. F. 2015, *MNRAS*, **449**, 3755
- Viganò, D., Torres, D. F., Hirovani, K., & Pessah, M. E. 2015, *MNRAS*, **447**, 2649
- ¹ Università di Udine, and INFN Trieste, 33100 Udine, Italy
- ² INAF National Institute for Astrophysics, 00136 Rome, Italy
- ³ Università di Siena, and INFN Pisa, 53100 Siena, Italy
- ⁴ Croatian MAGIC Consortium, Rudjer Boskovic Institute, University of Rijeka and University of Split, 10000 Zagreb, Croatia
- ⁵ Max-Planck-Institut für Physik, 80805 München, Germany
- ⁶ Universidad Complutense, 28040 Madrid, Spain
e-mail: dfidalgo@gae.ucm.es
- ⁷ Inst. de Astrofísica de Canarias, 38200 La Laguna, Tenerife, Spain
- ⁸ University of Łódź, 90236 Lodz, Poland
- ⁹ Deutsches Elektronen-Synchrotron (DESY), 15738 Zeuthen, Germany
- ¹⁰ ETH Zurich, 8093 Zurich, Switzerland
- ¹¹ IFAE, Campus UAB, 08193 Bellaterra, Spain
- ¹² Universität Würzburg, 97074 Würzburg, Germany
- ¹³ Centro de Investigaciones Energéticas, Medioambientales y Tecnológicas, 28040 Madrid, Spain
- ¹⁴ Institute of Space Sciences (CSIC-IEEC), 08193 Barcelona, Spain
e-mail: wilhelmi@aliga.ieec.uab.es
- ¹⁵ Università di Padova and INFN, 35131 Padova, Italy
- ¹⁶ Technische Universität Dortmund, 44221 Dortmund, Germany
- ¹⁷ Unitat de Física de les Radiacions, Departament de Física, and CERES-IEEC, Universitat Autònoma de Barcelona, 08193 Bellaterra, Spain
- ¹⁸ Universitat de Barcelona, ICC, IEEC-UB, 08028 Barcelona, Spain
e-mail: robertazanin@gmail.com, dgalindo@am.ub.es
- ¹⁹ Japanese MAGIC Consortium, Division of Physics and Astronomy, Kyoto University, Kyoto, Japan
- ²⁰ Academia Sinica, Institute of Astronomy and Astrophysics (ASIAA), PO Box 23-141, 10617 Taipei, Taiwan
- ²¹ Finnish MAGIC Consortium, Tuorla Observatory, University of Turku and Department of Physics, University of Oulu, 90014 Oulu, Finland
- ²² Inst. for Nucl. Research and Nucl. Energy, 1784 Sofia, Bulgaria
- ²³ Università di Pisa, and INFN Pisa, 56126 Pisa, Italy
- ²⁴ ICREA and Institute of Space Sciences, 08193 Barcelona, Spain
- ²⁵ Università dell'Insubria and INFN Milano Bicocca, Como, 22100 Como, Italy
- ²⁶ Now at Centro Brasileiro de Pesquisas Físicas (CBPF/MCTI), R. Dr. Xavier Sigaud, 150 – Urca, 22290-180 Rio de Janeiro – RJ, Brazil
- ²⁷ Now at NASA Goddard Space Flight Center, Greenbelt, MD 20771, and Department of Physics and Department of Astronomy, University of Maryland, College Park, MD 20742, USA
- ²⁸ Now at École polytechnique fédérale de Lausanne (EPFL), Lausanne, Switzerland
- ²⁹ Now at Finnish Centre for Astronomy with ESO (FINCA), Turku, Finland
- ³⁰ Also at INAF-Trieste, Italy
- ³¹ Also at ISDC – Science Data Center for Astrophysics, 1290, Versoix, Geneva, Switzerland